Bidirectional reflectance function for oceanic waters with varying chlorophyll concentrations: Measurements versus predictions

Kj Voss, A Morel

▶ **To cite this version:**

Kj Voss, A Morel. Bidirectional reflectance function for oceanic waters with varying chlorophyll concentrations: Measurements versus predictions. Limnology and Oceanography, 2005, 50 (2), pp.698-705. 10.4319/lo.2005.50.2.0698 . hal-03494223

HAL Id: hal-03494223
https://hal.science/hal-03494223v1

Submitted on 26 Sep 2024

HAL is a multi-disciplinary open access archive for the deposit and dissemination of scientific research documents, whether they are published or not. The documents may come from teaching and research institutions in France or abroad, or from public or private research centers.

L'archive ouverte pluridisciplinaire **HAL**, est destinée au dépôt et à la diffusion de documents scientifiques de niveau recherche, publiés ou non, émanant des établissements d'enseignement et de recherche français ou étrangers, des laboratoires publics ou privés.

Distributed under a Creative Commons Attribution 4.0 International License

Limnol. Oceanogr., 50(2), 2005, 698–705
© 2005, by the American Society of Limnology and Oceanography, Inc.

Bidirectional reflectance function for oceanic waters with varying chlorophyll concentrations: Measurements versus predictions

Kenneth J. Voss
Department of Physics, University of Miami, Coral Gables, Florida 33124

André Morel
Laboratoire d'Oceanographie de Villefranche, Université Pierre et Marie Curie et Centre National de la Recherche Scientifique, BP 8, F 06238 Villefranche-sur-mer, France

Abstract

The bidirectional reflectance of the ocean is an important parameter in ocean color remote sensing. Model predictions for case-1 waters were compared with measurements over a large range of chlorophyll concentrations (0.1–10 mg m^{-3} Chl, where Chl represents the sum of chlorophyll *a* and phaeophytin *a*), but with restricted solar zenith angles. We used the measured chlorophyll concentration and a model to predict the shape of the upwelling spectral radiance distribution. We found that the model predicted the radiance in the view direction, normalized by the nadir radiance, to within 7%. We also found that $Q(E_u/L_u)$ was predicted within 7%.

The upward radiance field within oceanic waters is not isotropic, especially near the surface, where it depends strongly on the sun's position. The radiances in near-horizontal directions always exceed the nadir radiance, and the horizontal radiances toward the sun (dominated by forward scattering) are always greater than in the antisolar direction (back scattering). Notwithstanding that multiple scattering occurs within the medium and thus tends to homogenize the radiant field, the polar and azimuthal asymmetries persist throughout the upper layers of the ocean. The experimental evidence of this phenomenon dates back to the end of the 1950s and 1960s (Jerlov and Fukuda 1960; Tyler 1960; Sasaki et al. 1962); yet, the theoretical analysis and modeling of the upwelling light field has been undertaken more recently (Morel and Gentili 1991, 1993, 1996). The quantitative study of this anisotropy, essentially based on theory and computations, has been prompted by the implication of this phenomenon in the ocean color remote sensing problem, in so far as the radiance emerging from the ocean depends on the bidirectional structure of the upward radiance field just beneath the interface. With the development of new instrumentation (Voss 1989*a*; Voss and Chapin 1992), measurements of the radiance distribution at sea have been resumed after a long interruption (Voss 1989*b*; Voss et al. 2003).

The anisotropic character of the upward radiance field is conveniently expressed by the bidirectional function, or *Q*-function (Austin 1974), by which any upward radiance L_u is related to the planar upward irradiance E_u through

$$L_u(\theta_s, \theta', \varphi, \lambda) = \frac{E_u(\theta_s, \lambda)}{Q(\theta_s, \theta', \varphi, \lambda)} \quad (1)$$

where θ_s is the zenith-sun angle (in air), θ' is the angle between the nadir direction and the direction from which the upward radiance originates (in water); φ is the azimuth difference between the half planes containing the sun and the radiance, respectively ($\varphi = 0°$ corresponds to the sun's direction and 180° to the antisolar direction), and λ is the wavelength. The upward (planar) irradiance is obtained by integrating the radiance field over all upward directions (over the half space Ξ_u, with θ' from 0 to $\pi/2$, and φ from 0 to $\pm\pi$), according to

$$E_u(\theta_s, \lambda) = \int_{\Xi u} L_u(\theta_s, \theta', \varphi, \lambda)\cos\,\theta'\,d\omega. \quad (2)$$

Were the upward radiance field isotropic (L_u constant for all θ' and φ), *Q* would equal π. In natural waters, however, $Q(\theta_s, \theta', \varphi)$ may be well below or above π. Indeed, this function (an apparent optical property, AOP, sensu Preisendorfer 1961) depends on the geometry of illumination along with the inherent optical properties (IOPs) of the medium and the depth of the medium. Here, only the $Q(\theta_s, \theta', \varphi)$ values for the near-surface layer will be measured and considered.

The inherent optical properties determining the radiance distribution can be reduced to two properties: the single scattering albedo, ϖ (=b/c, the ratio of the scattering coefficient to the attenuation coefficient), and the volume scattering function $\beta(\psi)$, where ψ denotes the scattering angle. $\beta(\psi)$ itself results from the sum of the molecular water scattering function, $\beta_w(\psi)$, and the scattering function, $\beta_p(\psi)$, due to particles in suspension. At a given wavelength, $\beta_w(\psi)$ is a physical constant. In contrast, the magnitude and shape of $\beta_p(\psi)$ depends on the particle concentration and properties. Once the IOPs of the medium are known or assumed, the radiative transfer equation (RTE) can be solved, and the variations of the *Q*-function can be predicted for all geometrical configurations. Even if the RTE can be solved very accurately (Mobley et al. 1993), the predictive skill of such a model heavily depends on the quality (i.e., the degree of realism) of the IOPs used as inputs. For the particular problem of predicting the bidirectional properties of the upward

Acknowledgments

This work was supported by NASA (K.V.), ONR (K.V.), and ESA (A.M.). We also thank Dennis Clark and his group at NOAA/NESDIS for the cruise opportunity and the support of the crew of the RV *Melville* and Al Chapin for their help during the data collection.

radiant field, the shape of $\beta(\psi)$, particularly in the backward directions, is of paramount importance.

Motivations of the present study—Theoretical predictions have preceded, at least by their systematic nature, the scarce and rather difficult experimental determinations. A first series of computations (Morel and Gentili 1991, 1993) were presented, which were based on a bio-optical model of IOPs related to the chlorophyll concentration (Chl, the sum of chlorophyll *a* and phaeophytin *a*) in case-1 waters (Morel 1988). The adoption in this model of a single, normalized particulate volume scattering function, namely the Petzold–Mobley phase function (Mobley 1994), was regularly acknowledged as being a weakness. In effect, this phase function exhibits a high backscattering efficiency (1.8%). This efficiency leads to unrealistic (namely too high) values for the backscattering coefficient, and consequently for reflectance, in waters when the chlorophyll content is high. In such cases as the influence of particles becomes preponderant (compared with that of molecules), the overestimate of the backscattering efficiency has a direct impact. Therefore, the first published modeled values of the *Q*-function were considered as becoming questionable when Chl $\geq$ 1 mg m^{-3}.

Nevertheless, within the domain of their validity (Chl $<$ 1 mg m^{-3}), these computed *Q*-values for all upward directions were successfully compared with experimental determinations of the same *Q*-function, which were performed using an electro-optic radiance distribution camera system (Voss 1989*a*). These in situ measurements were carried out in Californian waters, with Chl steadily around 0.3 mg m^{-3}, while the sun–zenith angle, θ_s, varied over a wide range (between 32° and 80° in a clear, cloud-free sky condition). The excellent agreement (Morel et al. 1995) remains, up to now, the unique instance of a direct validation of theoretical predictions, yet are restricted to low Chl waters and to a single instance in terms of chlorophyll concentration.

To remove the model limitation mentioned above, the IOP model for case-1 waters has been modified (Morel et al. 2002) by introducing a particle phase function that is now slightly dependent on Chl. In this way, the particle backscattering efficiency is no longer a constant, but decreases from about 1.4% down to 0.19%, when Chl increases from 0.01 up to 10 mg m^{-3}. This revised model also accounts for the Raman scattering emission. Based on this model, the *Q*-function (and other parameters associated with reflectance) could, in principle, be predicted for the full Chl range. The results of this revised model are practically unchanged (compared with those of the previous computations) when dealing with low Chl values; but they can now extend to Chl concentrations larger than 1 mg m^{-3}. These results are still only theoretical predictions that rely on the adopted parameterization for the IOPs.

Therefore, the purpose of the present article is to compare these newly computed *Q*-values with recent in situ determinations performed in various case-1 waters that encompass a wide range of chlorophyll concentrations.

Data and methods

Field determinations—The radiance distribution data used in this study were obtained in the vicinity of Baja California, Mexico, during a cruise on the RV *Melville* over the period of 01 October 1999–21 October 1999. Figure 1 shows the station locations for the radiance distribution data included in this study. While there were a total of 20 stations during this cruise, only cloud-free, case-1 stations were included. The stations used in this study are described in Table 1.

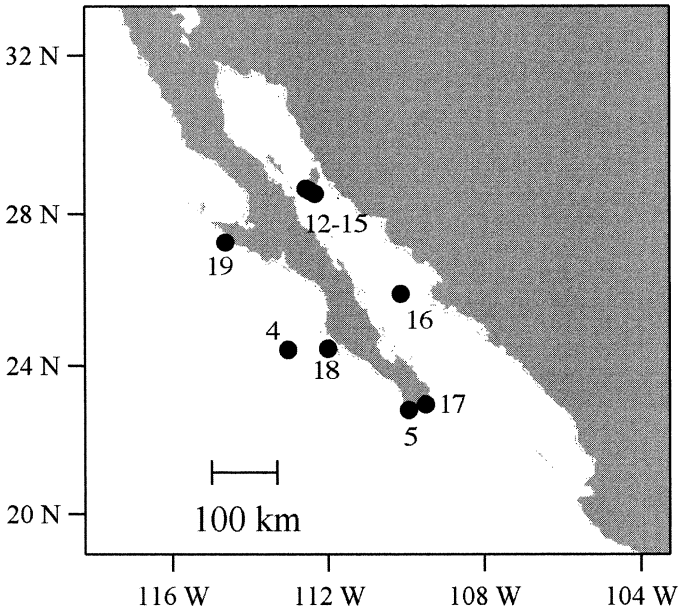

Fig. 1. Map of station locations used in this article. Stations were located in the Gulf of California and around the Baja Peninsula.

This cruise provided an opportunity to sample the upwelling radiance distribution over a wide range of chlorophyll concentrations (from 0.14 to 11.4 mg m^{-3}, for the surface layer). Because the main purpose of the cruise was satellite validation, the station times were determined by the satellite overpass times. Thus, stations occurred at roughly the same time each day and the variation in solar zenith angles was not large (only 28–40°). The wind was mostly less than 3 m s^{-1} and the sea state was relatively calm.

The radiance distribution camera system (RADS-II [Voss and Chapin 1992]) includes both up- and downwelling radiance distribution sensors, along with up- and downwelling irradiance collectors. The radiance distribution sensors are based on fisheye lenses, as in Smith et al. (1970), but cooled electronic cameras are used rather than film cameras. In addition, a filter changer is included in the optical train to allow the radiance distribution to be sampled at four wavelengths (440, 490, 560, and 670 nm). The instrument has an internal computer and hard drive to provide local control for the camera and store the camera images. For these measurements, the instrument was floated with a round 0.5-m fender, with the measurement depth at approximately 1.5 m. The instrument was connected to the ship by an umbilical cable and was allowed to float approximately 30 m or more from the ship. This allowed the measurements to avoid effects from the ship shadow. In most cases, the sun was off of the beam of the ship, minimizing the ship shadow effect in the

19395590, 2005, 2, Downloaded from https://aslopubs.onlinelibrary.wiley.com/doi/10.4319/lo.2005.50.2.0698 by Cochrane France, Wiley Online Library on [26/09/2024]. See the Terms and Conditions (https://onlinelibrary.wiley.com/terms-and-conditions) on Wiley Online Library for rules of use; OA articles are governed by the applicable Creative Commons License

data. When the instrument is retrieved, data are removed from the instrument over an Ethernet link.

Each measurement sequence for the RADS-II consists of alternating light and dark images at each wavelength. Because of time constraints, only two sets of images were obtained at each wavelength, for a total of 16 images (eight light images and eight associated dark images). Each image was reduced using the required calibration steps to obtain the upwelling radiance distribution (Voss and Zibordi 1989). For each image, the position of the plane of symmetry (i.e., the vertical plane containing the sun direction) was determined visually. The two images at each wavelength were averaged, along with each side of this symmetry plane. Thus, the angular data for each wavelength shown below are the average of four (half-hemispheres) radiance distributions. To compare the measurements with the model results, for each model nadir and azimuth angle, the average of a $4° \times 4°$ (full angle) box around this point was obtained. In addition, the average at the nadir position was used to normalize the other view directions.

We did not correct for the instrument self-shading effects (Gordon and Ding 1992; Doyle and Voss 2000). For the radiance distribution, to perform this correction would require exact knowledge of all of the in-water IOPs, including the light-scattering phase function. Because we did not have this information, the correction would probably introduce errors into the measurement. Instead, a simple geometrical model was developed to determine the extent of the directly shadowed volume. The instrument shape was taken to be a rectangular box (0.2 m on edge), with sides extending to the surface (1.5 m). The shadow region was approximated by assuming no scattering, an opaque instrument, simple illumination from the direct sunbeam, and a flat surface. The distance between the measurement point (assumed to be in the center of the lower surface of the box) and the edge of the shadow region was calculated. We then used the absorption, calculated from the model for the given Chl level (Morel and Maritorena 2001), and calculated the ratio of the self-shading error for a given direction to the self-shading error for the nadir look direction (because all data were normalized to this direction). If this predicted error was greater than 10%, we considered the data heavily shadowed and unusable. In addition, we also excluded data for which the nadir angle was greater than 15° and the azimuthal angle was greater than 160° (around the antisolar direction), which were obviously shadowed quite heavily. The shadowed data that are shown in Fig. 4 are excluded from Fig. 5.

The Chl concentration profile for each station was measured before or after the radiance distribution data were collected. Water samples were obtained at discrete depths in a bottle cast and the Chl determined by the fluorometric method (Strickland and Parsons 1972; Trees et al. 2003). These Chl profiles were linearly interpolated at 1-m increments, then a model was used to generate a $K_d(\lambda, z)$ profile from the Chl profile (Morel and Maritorena 2001). $K_d(\lambda, z)$ was used to determine *z90,* the penetration depth (Gordon and McCluney 1975), and this was combined with the $K_d(\lambda, z)$ and Chl profiles to determine the weighted average of the Chl ($\overline{\text{Chl}}$) by the equation (Gordon and Morel 1983)

Table 1. Specifications of stations used in this analysis. The asterisks denote the experiments (stations and specific wavelengths) selected for Figure 1.

Station No.	Solar zenith angle (°)	Wavelength (nm)	$\overline{Chl}$ (mg m^{-3})	Q_n (λ)	*z90* (m)
4	30	440	0.17	3.51	25.6
		490	0.18	3.67	33.7
		560	0.15	3.49	13.8
		670	0.14	3.72	2.7
5	28	440	0.39	3.61	14.4
		490	0.37	3.69	20.6
		560	0.40	3.73	11.8
		670	0.43	3.57	2.6
12	37	440	9.94	4.66	1.7
		490	9.33	4.73	2.5
		560	8.02	4.86	4.2
		670*	10.02	3.92	1.6
13	37	440*	8.93	4.33	1.8
		490	8.21	4.45	2.7
		560	6.85	4.55	4.4
		670	9.01	3.66	1.7
14	37	440	7.65	4.49	2.2
		490	7.62	4.56	3.1
		560*	7.56	4.61	4.7
		670	7.67	3.78	1.8
15	40	440	6.98	4.79	2.3
		490	7.06	4.66	3.4
		560	7.17	4.81	4.9
		670	6.94	3.58	1.8
17	40	440	0.62	3.71	18.7
		490*	0.95	3.74	22.7
		560	0.35	3.72	13.3
		670	0.17	3.57	2.7
18	34	440	0.32	3.53	18.9
		490	0.42	3.59	25
		560	0.27	3.66	12.9
		670	0.24	3.51	2.6
19	38	440*	1.98	4.12	5.5
		490	1.99	4.19	7.8
		560	1.99	4.32	8
		670	1.96	3.79	2.3

$$\overline{Chl} = \int_0^{z90} Chl(z) f(z, \lambda)\, dz \Big/ \int_0^{z90} f(z, \lambda)\, dz \qquad (3)$$

where

$$f(z, \lambda) = \exp\left[-2 \int_0^z K_d(z', \lambda)\, dz'\right] \qquad (4)$$

Because K_d is spectrally dependent, *z90* and $\overline{\text{Chl}}$ were also spectrally dependent. *z90* and $\overline{\text{Chl}}$ for each wavelength are listed in Table 1.

Model–The *f*/*Q*-tables, described in Morel et al. (2002), are available over the Internet at oceane.obs-vlfr.fr in pub/gentili/AppliedOptics2002. To find the corresponding $f/Q(\theta_s, \theta', \Delta\varphi)$ for the individual experimental cases, the tables were interpolated using $\log(\overline{\text{Chl}})$ and $\cos(\theta_s)$. By taking the ratio of $[f/Q(\theta_s, \theta', \Delta\varphi)]/[f/Q(\theta_s, 0, 0)]$, one can obtain the ratio

$$L_u(\theta_s, \theta', \Delta\varphi)/L_u(\theta_s, 0, 0) \qquad (5)$$

19395590, 2005, 2, Downloaded from https://aslopubs.onlinelibrary.wiley.com/doi/10.4319/lo.2005.50.2.0698 by Cochrane France, Wiley Online Library on [26/09/2024]. See the Terms and Conditions (https://onlinelibrary.wiley.com/terms-and-conditions) on Wiley Online Library for rules of use; OA articles are governed by the applicable Creative Commons License

The particular Q value for the nadir direction, simply denoted Q_n (actually, it is $Q_n[\theta_s, 0, 0]$), can be computed straightforwardly by:

$$Q_n(\theta_s, \lambda, \overline{Chl}) = Q_0(0, \lambda, \overline{Chl}) + S_{Q_n}(\lambda, \overline{Chl})[1 - \cos(\theta_s)] \quad (6)$$

where $Q_o(0, \lambda, \overline{\text{Chl}})$ and $S_{Qn}(\lambda, \overline{\text{Chl}})$ can be interpolated from Table 2 in Morel et al. (2002). Note that the factor f (which disappears in the above ratio, and is not used for the present study) relates the irradiance reflectance to the IOPs (namely the absorption and backscattering coefficients).

Results and first discussion

To start the analysis, Q_n, as derived from the data, are compared with those produced by the model using as inputs $\overline{\text{Chl}}$ and θ_s. This comparison, for each considered wavelength, is shown in Fig. 3A–D. Overall, the comparison, for the wavelengths 440, 490, and 560 nm, is quite good. The general increase in Q_n with $\overline{\text{Chl}}$ (cf., Fig. 9 in Morel et al. 2002) is clearly shown in both the measurements and the theoretical computations, despite some noise. There appears to be an offset between the experiment and model of 0.27 $\pm$ 0.02, which is less than 8% of the total Q_n, well within the error budget of calculating E_u (hence Q_n) from the data. Because E_u requires an integral out to the horizon and because this area of the image is highly affected by the calibration due to lens rolloff (Voss and Zibordi 1989), it contains more error than L_u (θ_s, θ', φ, λ) for the central angles that are transmitted through the sea–air interface. The agreement is obviously not as good for Q_n(670 nm). Here, the data are contaminated by shadowing at all chlorophyll concentrations because of the high absorption coefficient of the water itself. The upwelling irradiance is affected more than the upwelling nadir radiance, thus Q_n is depressed.

Analyzing their data obtained in clear (low Chl) waters, Aas and Hojerslev (1999) predicted that Q_n (at blue wavelengths and at 5 m depth) should follow either

$$Q_n = 5.33 \exp[-0.45 \cos(\theta_s)], \quad \text{or} \quad (7)$$

$$Q_n = 5.20 - 1.82 \cos(\theta_s) \quad (8)$$

For the present data set, θ_s in the clear-water stations ranged from about 30° to 40°. Thus, the range of Q would be 3.61–3.77 (through Eq. 7) and 3.62–3.80 (Eq. 8). Figure 3A and B shows that the low-$\overline{\text{Chl}}$ cases (<0.4 mg m^{-3}) in our data set agree with either of these formulations. The Q_n factor has also been determined for various wavelengths in the North Adriatic Sea (Zibordi and Berthon 2001). In these optically complex coastal waters, the observed Q_n values were generally high and similar to those observed here for high $\overline{\text{Chl}}$. The comparison cannot be carried further because of the differing optical properties between such coastal waters and case-1 waters.

The detailed spatial distribution of the upward radiances, either predicted or measured, are jointly displayed in Fig. 4. While there were more than 30 sample sets to work with, it is impractical to show them all in detail. We chose five examples that were neither better nor worse than the others not displayed. These examples show a sample at each wavelength and for 440 nm at both high and low $\overline{\text{Chl}}$ (to illustrate the span of $\overline{\text{Chl}}$ in the present data set). However, the entire data set will be shown in Fig. 5.

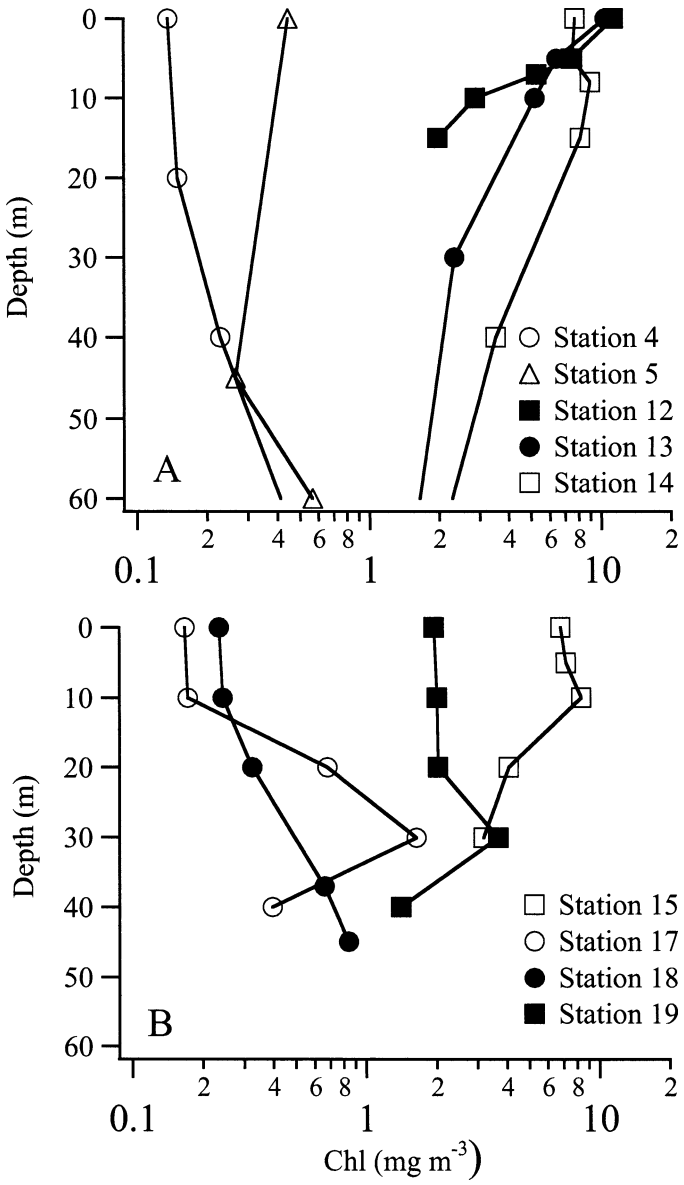

Fig. 2. Chlorophyll concentration profiles for the stations used in this study. (A) Sta. 4–14, (B) Sta. 15–19.

Instead of plotting directly the Q-factors, the polar graphs (Fig. 4) show a relative quantity, namely, the ratio of slant radiances to the nadir radiance; this ratio also represents (cf., Eq. 1) the inverse ratio of the Q-quantities, according to

$$\frac{L_u(\theta_s, \theta', \varphi)}{L_{u,nadir}(\theta_s, 0, 0)} = \frac{Q_n(\theta_s)}{Q(\theta_s, \theta', \varphi)}. \quad (9)$$

In the polar plots in Fig. 4, the isolines, corresponding to discrete values of this ratio, are drawn inside the external circle, which corresponds to $\theta' = 50°$, (slightly larger than the critical angle); all the upward radiances able to emerge from the water (assuming a flat surface) are thus captured

19395590, 2005, 2, Downloaded from https://aslopubs.onlinelibrary.wiley.com/doi/10.4319/lo.2005.50.2.0698 by Cochrane France, Wiley Online Library on [26/09/2024]. See the Terms and Conditions (https://onlinelibrary.wiley.com/terms-and-conditions) on Wiley Online Library for rules of use; OA articles are governed by the applicable Creative Commons License

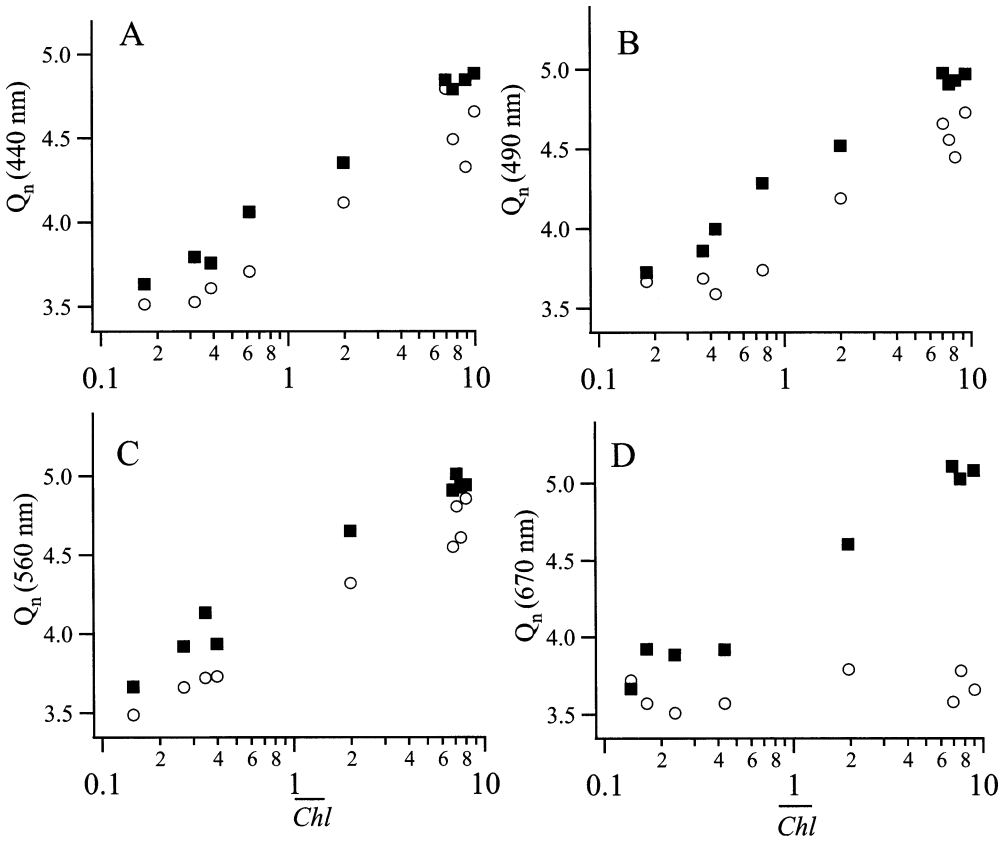

Fig. 3. Q_n (the particular Q value for nadir direction) as a function of $\overline{\text{Chl}}$. (A) 440 nm, (B) 490 nm, (C) 560 nm, and (D) 670 nm. Data are shown as the open circles while the model values are shown as the filled squares.

in this representation. The data are shown on the left side of the polar graph while the model predictions, for the specified $\overline{\text{Chl}}$ and θ_s, are shown on the right. The shadowed zone in the vicinity of the antisolar direction is clearly seen (on the left side of these graphs) for azimuth angles beyond ~135° and is particularly obvious at the red wavelength (Fig. 4A).

A closer comparison between data and modeled values is provided by the cartesian graphs in Fig. 4, where the relative percentage differences (100%[data − model]/model) are displayed as a function of azimuth and nadir angles. The simple approximation of the shadow error is illustrated by the bold, black contour line on the right of each panel. This line delineates the threshold corresponding to a 10% error; the area to the right of this line (toward 180° azimuth) would experience a larger shadow error, the area to the left a smaller shadow error. This approximate approach probably underestimates the shadow zone in the red wavelength. Outside of the shadow, the differences are small and generally less than 7%. As expected, considerable negative differences occur inside the shadow zone and the angular domain affected by this artifact is rather wide. It corresponds to about ±45° on both sides of the antisolar direction and from about 10° to 50° in nadir angle, with a maximum around $\theta' = 20$–25°. This is in keeping with the three-dimensional structure of the camera itself, and, accordingly, with its three-dimensional shadow. Its vertical structure explains that the maximal (negative) difference is generally not found in the θ_s' direction, which corresponds to the refracted antisolar direction, but at a slightly larger nadir angle. The intensity of the shadow depends on external conditions, namely, the relative proportions of the diffuse sky radiation and the direct sun radiation and the sea surface state, as well as on internal processes, essentially multiple scattering and absorption (or ϖ) values. The shadow is systematically more intense in high $\overline{\text{Chl}}$ waters and in the red part of the spectrum (about −44% at 670 nm, Sta. 15) and weakens (for instance, −10% at 440 and 490 nm, Sta. 17) for blue radiation and in clear waters, where the molecular scattering, with its nearly isotropic phase function, predominates. In such waters, the filling in of the shadow is more efficient than it can be when strongly forward-peaked phase functions redirect the photons, which is the case in high $\overline{\text{Chl}}$, heavily particle-loaded waters.

Figure 5 illustrates the model versus data for all stations merged into two groups, namely $0.1 < \overline{\text{Chl}} < 1$, and $1 < \overline{\text{Chl}} < 10$. Data from the shadow region are excluded in these graphs. There is an obvious difference in the values of the ratio $L_u(\theta', \Delta\varphi)/L_{u,nadir}$ (both measured or modeled values) according to the $\overline{\text{Chl}}$ range considered. Actually, this ratio remains confined within a narrow interval (0.97–1.25) when $0.1 < \overline{\text{Chl}} < 1$ mg m^{-3} and when Q_n is low (Fig. 3) and thus $L_{u,nadir}$ is high; in contrast, this ratio may reach 2 for high-$\overline{\text{Chl}}$ waters (when Q_n is maximal and thus $L_{u,nadir}$ minimal). In the low-$\overline{\text{Chl}}$ case, and due to the restricted range of variation, the scatter of the

19395590, 2005, 2, Downloaded from https://aslopubs.onlinelibrary.wiley.com/doi/10.4319/lo.2005.50.2.0698 by Cochrane France, Wiley Online Library on [26/09/2024]. See the Terms and Conditions (https://onlinelibrary.wiley.com/terms-and-conditions) on Wiley Online Library for rules of use; OA articles are governed by the applicable Creative Commons License

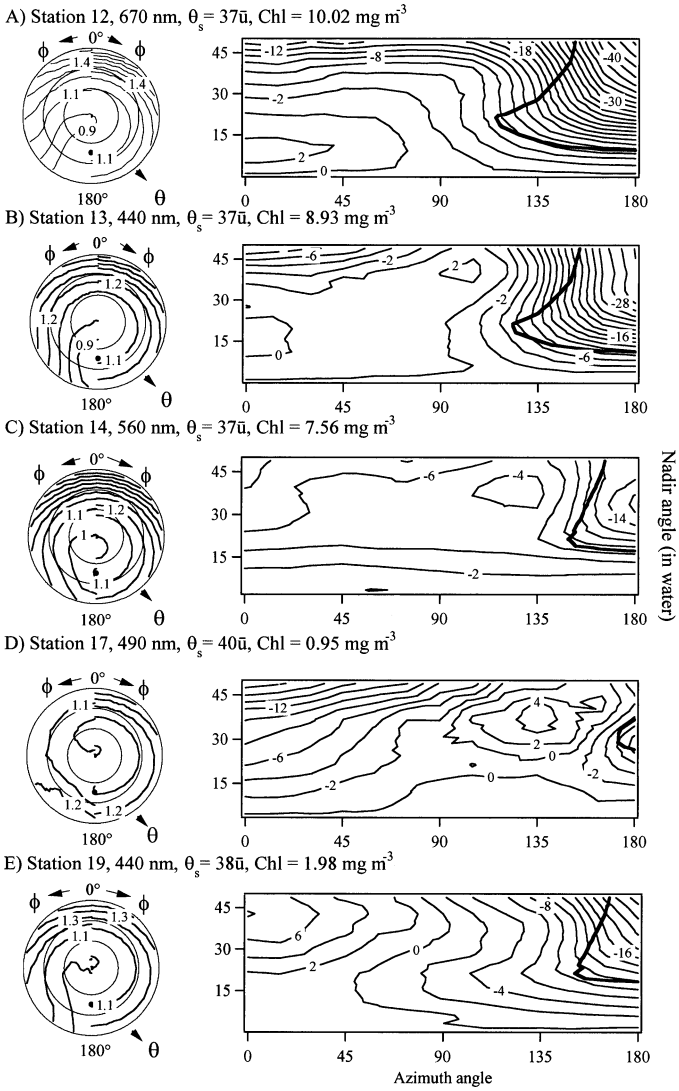

Fig. 4. On the left (circular plots) are polar comparisons of model versus data; the data are displayed in the left hemisphere and the model is displayed in the right hemisphere. Lines correspond to isolines of $L_u(\theta', \varphi)/L_u(0, 0)$. The in-water nadir angle is displayed as radius from the center (marked circles are at 20°, 35°, and 50°), while azimuthal angle is displayed around the circle; 0° in azimuth corresponds to the solar direction and 180° corresponds to the antisolar direction. A filled circle marks the refracted antisolar position. The rectangular plot on the right is 100 × (data − model)/model as a function of azimuth and nadir angle. This graph shows the quantitative difference between the data and predicted value. The bold contour shows where we estimate that the shadowing error is 10%. Shading is larger to the higher azimuth side of this line.

points appears more pronounced (with the expanded scales as adopted). This is particularly true for the wavelength 670 nm. Because of experimental difficulties due to the high water absorption in the red part of the spectrum (and self-shadowing effects), the data–model comparison is less convincing for the wavelength 670 nm for low-$\overline{\text{Chl}}$ values, although it is rather satisfactory for high-$\overline{\text{Chl}}$ values.

Discussion

Regarding the general structure of the upward light field (and discarding the shadow region), the polar diagrams, as well as their associated plots displaying the relative percent differences, demonstrate that an excellent agreement does exist between the data and the modeled values. As shown by Fig. 5, this quantitative agreement extends to all trophic situations and all wavelengths considered. The standard deviations of the percent difference between the model and measurements for 450, 490, and 560 nm combined are 5.0% for the $\overline{\text{Chl}}$, 6.7% for the high $\overline{\text{Chl}}$, and 6.0% for the combined data set.

As expected from theoretical considerations (Morel and Gentili 1996), the span of variations in the $L_u(\theta', \varphi)/L_{\text{nadir}}$ ratio, which is maximal for high $\overline{\text{Chl}}$ values, is also sensitive to the wavelength. When $\overline{\text{Chl}} \geq 1$ mg m^{-3}, it ranges from 1 to 1.8 at $\lambda = 440$ nm or from 1 to 2 at $\lambda = 560$ nm. The range of variations distinctly narrows for oligotrophic waters. With low $\overline{\text{Chl}}$, the upward radiance field tends to become almost isotropic, at least for high solar elevation.

Interestingly the minimal $L_u(\theta', \varphi)$ does not occur at nadir nor in the exact antisolar direction for all samples (in contrast with the predictions of Aas and Hojerslev 1999). At low $\overline{\text{Chl}}$ values, as evidenced by Sta. 17, 490 nm (Fig. 4D), the L_u minimum is actually in the solar plane toward the sun from nadir ($\varphi = 0$) and at a nadir angle $\theta' \approx 15°$. The model predicts and experimental measurements show that this minimum will move to the nadir at a $\overline{\text{Chl}}$ level of about 1.2 mg m^{-3} for 490 nm.

As has been shown, the radiances exiting a hypothetical perfectly uniform ocean, but seen under various angles and differing illumination conditions, are in no way constant. As a consequence, the normalized water-leaving radiances, $[L_w]_N$ (as defined in Gordon and Clark 1981) are still dependent on the geometry of observation. Therefore, one pixel cannot be coherently compared with another pixel within a scene, day to day, nor between sensors. The merging of such $[L_w]_N$ quantities is also problematic. Nevertheless, removing such inconsistencies generated by the bidirectional effects is possible and consists of transforming $[L_w]_N$ into the exact normalized water-leaving radiance, $[L_w]^{ex}_N$ (Morel and Mueller 2002). Such a transformation is practically effected through the use of appropriate lookup tables. These tables are derived from the same theoretical computations and the same IOP model for case-1 waters that have been used in the present study. Therefore, a comprehensive validation of this model, encompassing a wide range of chlorophyll concentration typical of most oceanic waters, was highly desirable. In coastal turbid waters, the bio-optical model does not apply so that the bidirectional correction is not feasible, even if some approximate solutions have been proposed (Loisel and Morel 2001). In any case, identifying the turbid case-2 waters through their high reflectance is rather easy (even from space) and can thus prevent the misuse of the bidirectional correction scheme as developed for case-1 waters.

The present validation is also important for another reason. The anisotropy within the upward radiance field is highly sensitive to the shape of the volume-scattering func-

19395590, 2005, 2, Downloaded from https://aslopubs.onlinelibrary.wiley.com/doi/10.4319/lo.2005.50.2.0698 by Cochrane France, Wiley Online Library on [26/09/2024]. See the Terms and Conditions (https://onlinelibrary.wiley.com/terms-and-conditions) on Wiley Online Library for rules of use; OA articles are governed by the applicable Creative Commons License

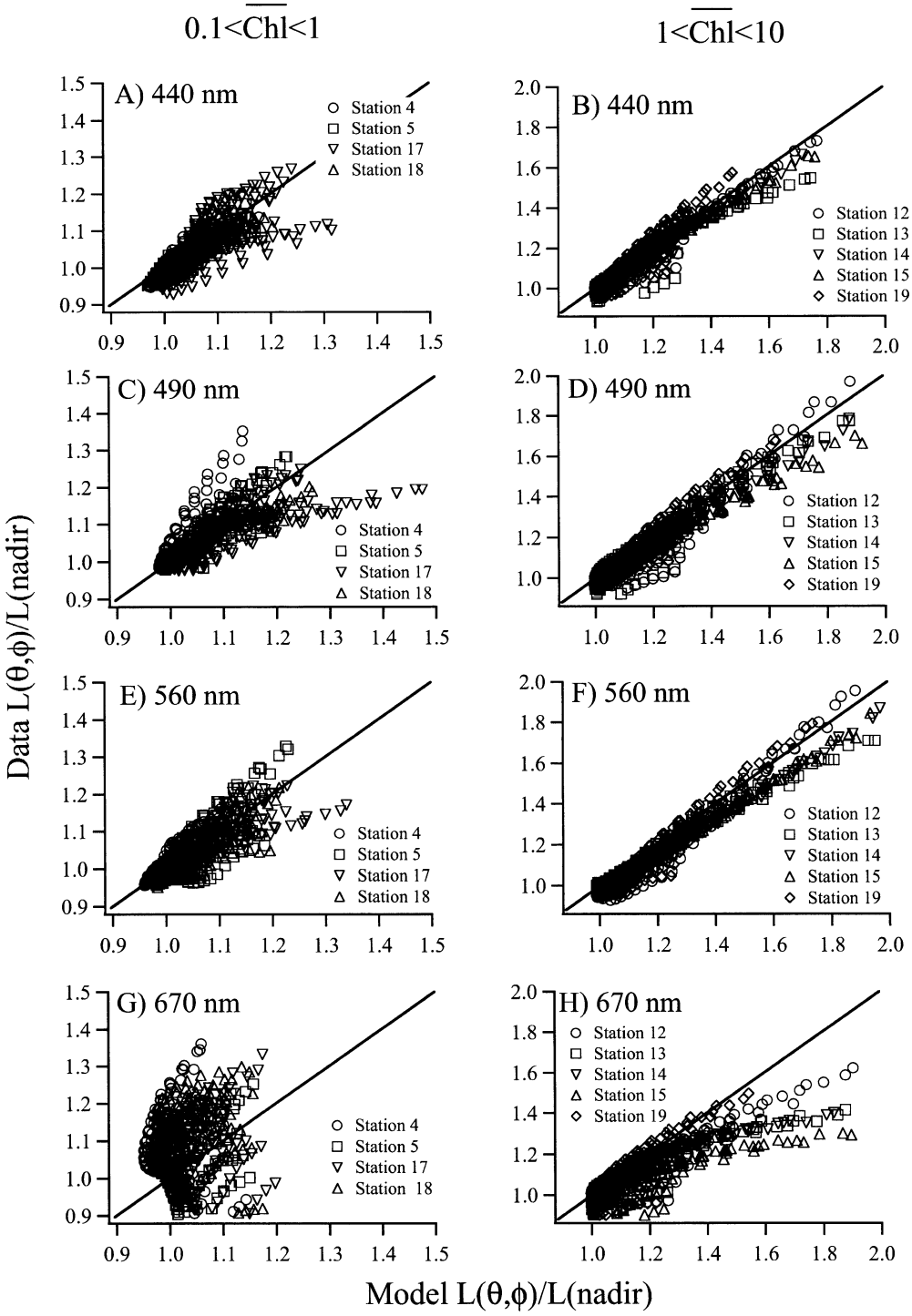

Fig. 5. Model versus data comparison for all stations separated into two major chlorophyll concentrations (mg m^{-3}), 0.1; lt $\overline{Chl} < 1$ and $1 < \overline{Chl} < 10$, for 440, 490, 560, and 670 nm.

tion and particularly to its backward lobe. This function, and its variation with the chlorophyll concentration, is crucial for bio-optical modeling, yet still poorly documented. Therefore, the present validation via the comparison of measured and predicted upward radiance fields is of considerable value.

References

AAS, E., AND N. K. HOJERSLEV. 1999. Analysis of underwater radiance distribution observations: Apparent optical properties and analytical functions describing the angular radiance distributions. J. Geophys. Res. **104:** 8015–8024.

AUSTIN, R. W. 1974. The remote sensing of spectral radiance from

19395590, 2005, 2, Downloaded from https://aslopubs.onlinelibrary.wiley.com/doi/10.4319/lo.2005.50.2.0698 by Cochrane France, Wiley Online Library on [26/09/2024]. See the Terms and Conditions (https://onlinelibrary.wiley.com/terms-and-conditions) on Wiley Online Library for rules of use; OA articles are governed by the applicable Creative Commons License

below the ocean surface, p. 317–344. *In* N. G. Jerlov and E. S. Nielsen [eds.], Optical aspects of oceanography. Academic.

Doyle, J. P., and K. J. Voss. 2000. 3D instrument self-shading effects on in-water multi-directional radiance measurements. Ocean Optics XV, Monaco, October 16–20.

Gordon, H. R., and D. K. Clark. 1981. Clear water radiances for atmospheric correction of Coastal Zone Color Scanner imagery. Appl. Opt. **20:** 4175–4180.

———, and K. Ding. 1992. Self-shading of in-water optical instruments. Limnol. Oceanogr. **37:** 491–500.

———, and W. R. McCluney. 1975. Estimation of the depth of sun light penetration in the sea for remote sensing. Appl. Opt. **14:** 413–416.

———, and A. Morel. 1983. Remote assessment of ocean color for interpretation of satellite visible imagery: A review. Springer-Verlag.

Jerlov, N. G., and M. Fukuda. 1960. Radiance distribution in the upper layers of the sea. Tellus **12:** 348–355.

Loisel, H., and A. Morel. 2001. Non-isotropy of the upward radiance field in typical coastal (case-2) waters. Int. J. Remote Sensing **22:** 275–295.

Mobley, C. D. 1994. Light and Water, Academic Press.

———, and others. 1993. Comparison of numerical models for computing underwater light fields. Appl. Opt. **32:** 7484–7504.

Morel, A. 1988. Optical modeling of the upper ocean in relation to its biogenous matter content (case-1 waters). J. Geophys. Res. **93:** 10749–10768.

———, D. Antoine, and B. Gentili. 2002. Bidirectional reflectance of oceanic waters: Accounting for Raman emission and varying particle scattering phase function. Appl. Opt. **41:** 6289–6306.

———, and B. Gentili. 1991. Diffuse reflectance of oceanic waters: its dependence on sun angle as influenced by the molecular scattering contribution. Appl. Opt. **30:** 4427–4438.

———, and ———. 1993. Diffuse reflectance of oceanic waters. II. Bidirectional aspects. Appl. Opt. **32:** 6864–6879.

———, and ———. 1996. Diffuse reflectance of oceanic waters. III. Implication of bidirectionality for the remote sensing problem. Appl. Opt. **35:** 4850–4862.

———, and S. Maritorena. 2001. Bio-optical properties of oceanic waters: A reappraisal. J. Geophys. Res. **106:** 7163–7180.

———, and J. L. Mueller. 2002. Normalized water-leaving radiance and remote sensing reflectance: Bidirectional reflectance and other factors, p. 183–210. *In* J. L. Mueller and G. S. Fargion [eds.], Ocean optics protocols for satellite ocean color sensor validation, Rev. 3, V. 2. NASA/TM, Goddard Space Flight Center.

———, K. J. Voss, and B. Gentili. 1995. Bi-directional reflectance of oceanic waters: A comparison of model and experimental results. J. Geophys. Res. **100:** 13143–13150.

Preisendorfer, R. W. 1961. Application of radiative transfer theory to light measurements in the sea. Intl. Union Geod. Geophys. Monograph 10: 11–39.

Sasaki, T., S. Watanabe, G. Oshiba, N. Okami, and M. Kajihara. 1962. On the instrument for measuring angular distribution of underwater radiance. Bull. Japan. Soc. Sci. Fisheries **28:** 489–496.

Smith, R. C., R. W. Austin, and J. E. Tyler. 1970. An oceanographic radiance distribution camera system. Appl. Opt. **9:** 2015–2022.

Strickland, J. D. H., and T. R. Parsons. 1972. A practical handbook of sea water analysis. Fisheries Research Board of Canada.

Trees, C. C., R. R. Bidigare, D. M. Karl, L. Van Heukelem, and J. Dore. 2003. Fluorometric chlorophyll a: Sampling, laboratory methods, and data analysis protocols, p. 15–20. *In* J. Mueller, G. Fargion, and C. McClain, [eds.], Ocean optics protocols for satellite ocean color sensor validation, Rev. 5, V. 5. NASA TM, Goddard Space Flight Center.

Tyler, J. E. 1960. Radiance distribution as a function of depth in an underwater environment. Bull. Scripps Inst. Oceanogr. **7:** 363–41.

Voss, K. J. 1989*a.* Electro-optic camera system for measurement of the underwater radiance distribution. Optical Eng. **28:** 241–247.

———. 1989*b.* Use of the radiance distribution to measure the optical absorption coefficient in the ocean. Limnol. Oceanogr. **34:** 1614–1622.

———, and A. L. Chapin. 1992. Next generation in-water radiance distribution camera system. Proc. Soc. Photo-Opt. Instrument. Eng. **1759:** 384–387.

———, C. D. Mobley, L. K. Sundman, J. Ivey, and C. Mazell. 2003. The spectral upwelling radiance distribution in optically shallow waters. Limnol. Oceanogr. **48:** 364–373.

———, and G. Zibordi. 1989. Radiometric and geometric calibration of a spectral electro-optic ''fisheye'' camera radiance distribution system. J. Atmosph. Ocean. Technol. **6:** 652–662.

Zibordi, G., and J.-F. Berthon. 2001. Relationships between *Q*-factor and seawater optical properties in a coastal region. Limnol. Oceanogr. **46:** 1130–1140.

Received: 9 June 2004
Accepted: 15 September 2004
Amended: 30 September 2004

19395590, 2005, 2, Downloaded from https://aslopubs.onlinelibrary.wiley.com/doi/10.4319/lo.2005.50.2.0698 by Cochrane France, Wiley Online Library on [26/09/2024]. See the Terms and Conditions (https://onlinelibrary.wiley.com/terms-and-conditions) on Wiley Online Library for rules of use; OA articles are governed by the applicable Creative Commons License